IEEE Access
Multidisciplinary | Rapid Review | Open Access Journal

Received March 26, 2019, accepted April 5, 2019, date of publication April 18, 2019, date of current version April 30, 2019.

Digital Object Identifier 10.1109/ACCESS.2019.2912119

Optimum Wideband High Gain Analog Beamforming Network for 5G Applications

ESSA H. MUJAMMAMI, (Graduate Student Member, IEEE), ISLAM AFIFI, (Graduate Student Member, IEEE), AND ABDELRAZIK B. SEBAK, (Life Fellow, IEEE)
Electrical and Computer Engineering Department, Concordia University, Montreal, QC H4B 1R6, Canada
Corresponding author: Essa H. Mujammami (e_muja@encs.concordia.ca)

ABSTRACT A broadband high-gain millimeter-wave (mmWave) array beamforming network (BFN) design, analysis, and implementation based on the Rotman lens antenna array feeding are presented. The BFN is intended for operation in the (26–40) GHz frequency band for a wide range of potential applications in the fifth generation (5G). The system is made on Rogers substrate, RO6010, to provide compatibility with standard planar low-cost processing techniques for millimeter-wave monolithic integrated circuit (MMIC). The measured results show the system capability of 80° beam scanning for different angles at −39.7°, −26.5°, −13.3°, 0°, +13.3°, +26.5°, and +39.5° at 28 GHz. With these features in addition to being compact size, low profile, and lightweight, this BFN is suitable for various millimeter-wave and 5G applications such as the advanced multi-in multi-out (MIMO) systems, remote sensing, and automotive radar.

INDEX TERMS 5G antenna, automotive radar, beamforming, beam-switching, high gain, quasi-Yagi, remote sensing, Rotman lens.

I. INTRODUCTION

The next generation of wireless networks (5G) addresses the evolution of new kinds of network deployments beyond the current well-known wireless networks for the horizon 2020. 5G can handle far more traffic at much higher speeds than the base stations that make up for today's cellular networks such as 3G, 4G, and 4.5G (LTE advanced). More reliable services through ultra-dense radio networking, mesh-like connectivity, much higher bit rates, low latency, lower infrastructure cost, more efficient spectrum reuse, and much more, are the main characteristics of 5G. Therefore, advanced high gain antennas and BFNs are essential among many other design challenges are required for 5G [1]. Naturally, the propagation environment at millimeter wave (mmWave) frequencies, recommended for 5G, lends itself to a beamforming structure, where antenna arrays are required to obtain the necessary link budget. Thus, Analog beamforming (ABF), Digital beamforming (DBF), and Hybrid beamforming (HBF) architectures have been agreed to facilitate 5G evolution [2]. In fact, generating multiple RF beams using an array of antennas for mmWave systems is a crucial issue, where it should meet some challenging requirements. The BFN should have a wide-bandwidth and RF beam steering capability for a reasonable data rate in desired angular directions. Another issue is the compatibility with standard planar low-cost processing techniques for mmWave monolithic integrated circuit (MMIC) and high volume production [3]. The beamforming concept for the mmWave band is implemented using Butler matrix as reported in [4], [5]. However, Butler matrix is a narrow band system, due to its phase shifters [6]. In contrast, Rotman lens is a well-known beam scanning technique and is a true-time-delay (TTD) component. It provides beam steering independent of the frequency. Thus, it exhibits wideband properties. For its simple structure and cost-effective fabrication process, Rotman lens has been widely used in many applications such as satellite communication and remote sensing applications [7]–[9], radar systems for military applications [10], especially those fulfilling tracking and pointing tasks. It is, also, used for automotive radar sensing and adaptive cruise control [11], [12], imaging and security applications [13], and as a real-time spectrum-sniffer (RTSS) for cognitive radio [14].

Recently, Rotman has attracted much attention for use in 5G wireless networks. In [15], Rotman lens fed a wideband (25-30) GHz microstrip antenna array for use in 5G wireless

The associate editor coordinating the review of this manuscript and approving it for publication was Weiren Zhu.

communication applications is presented. The BFN is realized using a simple and low cost printed circuit board (PCB) technology to operate at 28 GHz with ($-40°$ to $+40°$) scanning range. However, the reported measured return loss indicates a poor matching performance ($S_{11} < -8.5$ dB). Another BFN with similar fabrication technology is presented in [16]. The basic idea is realizing a folded Rotman lens with the use of aperture coupling by multi-branch slots for the transition between the lens layers. In addition, rectangular slots are used to feed an array of patch antenna elements on the top layer. The BFN exhibits a scanning capability of $\pm 30°$ and good impedance matching between 26 GHz to 29 GHz with a maximum gain of 14 dBi. Although 50% size reduction is achieved, compared to the conventional Rotman lens, the multi-layer structure increases the overall thickness to 6 mm making it relatively bulky. Also, the use of patch antenna limits the bandwidth of the BFN. Substrate integrated waveguide (SIW) Rotman lens is presented in [17]–[20]. Seven beam ports and nine array ports Rotman lens for beam switching application is presented in [17]. The system has a scanning capability over $\pm 24°$ in X-band. Nevertheless, in SIW Rotman lens the distance between adjacent beam ports and adjacent array ports must be large to avoid interference between neighbor waveguides. Consequently, the lens size increases compared to PCB-based Rotman lens. More importantly, metallic vias deteriorate S-parameters and amplitude distribution on array elements [18]. A dual-layer Rotman lens with 50% size reduction, compared to a conventional one, is introduced in [19], [20] using SIW technology in the 24-GHz band. However, the multilayer structure and the size of $7.2\lambda_0 \times 12\lambda_0$ is electrically large. Furthermore, SIW Rotman lens-based beamforming or multibeam systems of [17]–[20] show a very narrowband performance ($\sim$4%-7%), which reduces the spectrum utilization of a TTD component such as Rotman lens. Alternatively, ridge gap waveguide (RGW) technology is proposed to realize Rotman lens for the advantage of only metal and air are used; therefore, the dielectric losses associated with PCB or SIW technologies are eliminated [21], [22]. An RGW Rotman lens is proposed in [23] for beam scanning in millimeter wave applications. The design shows a good performance in terms of S-parameters, especially the transition between RGW and WR28 in the input and output ports. However, 56 mm is needed just for transition section between RGW and WR28 for each input, or output port, in addition to 50 mm for the parallel plate region of Rotman lens results in a massive structure. Besides, to the authors' best knowledge, the physical implementation and measurement results of mmWave RGW Rotman lens are not reported yet in the open literature. Also, machining of such device in the mmWave band is exceptionally costly. Subsequently, there are some trials to reduce the implementation cost using metalized three-dimensional printing technology (3D-Printed) as reported in [21]. This might explain why only a few solutions have been reported so far to implement mmWave Rotman lens using RGW or 3D-Printed. Another possible technique is the printed version of RGW (PRGW), which is, by far, lower cost than RGW. In [24], PRGW Rotman lens operating at 60 GHz is proposed. The lens scanning range is $\pm 40°$. This solution reduces the dielectric losses, where the wave, in this case, propagates mainly in the air. However, the size of the BFN will increase, especially, when it is scaled for 28, or 38 GHz suggested for 5G [1] and also the use of air instead of a dielectric material increases, generally, the physical size. The inkjet processing technique is also possible for realizing Rotman lens with a low profile and low cost such as proposed in [25].

In this paper, seven-beam ports Rotman lens feeding eight Quasi-Yagi antenna array is implemented in the PCB technology. The proposed lens is designed to operate in the frequency band 26-40 GHz, where it is reported as one of the candidates for 5G wireless communications system for both indoor and outdoor devices [1], [26]. The lens is designed according to Hansen's design procedure for optimum Rotman lens parameters with maximum gain and minimum phase error [27]. The proposed work takes care of both the amplitude and the phase error at the same time to determine the design parameters of the proposed Rotman lens. The performance of the proposed BFN is compared to related beamforming systems with different fabrication technologies and exhibits a relatively high gain, broadband, and reasonable scanning performance in addition to being low-cost, low profile MMIC compatible.

The rest of the paper is organized as follows. Section II discusses the design procedure of Rotman lens based on Hansen's modification of original Rotman and Tuner equations and the optimization process in subsection A. A brief Rotman Lens design methodology is summarized in subsection B. Then, in subsection C, it addresses the design of the Quasi-Yagi antenna, the antenna that is used in the frontend of the proposed system. Section III shows the simulation results of the proposed BFN. A prototype of Rotman lens feeding eight Quasi-Yagi antennas, along with its measured results and discussion are presented in Section IV. The conclusion is presented in Section V.

II. ANALOG BEAMFORMING SYSTEM DESIGN CONFIGURATION THEORY AND ANALYSIS

In this work, Rogers 6010 substrate with dielectric constant of 10.2, loss tangent of 0.0023, and thickness of 0.381 mm is used in the design. Full-wave electromagnetic (EM) simulator CST ver. 16 has been adopted for the simulation.

A. ROTMAN LENS DESIGN CONFIGURATION

Rotman lens was invented in 1963 by Rotman and Turner [28]. Then, several methods were proposed to improve the performance of Rotman lens based on modifying the lens geometry or using optimization methods, e.g. [27], [29]–[31]. Hansen's modification of Rotman lens is used in this paper. A typical Rotman lens has M-beam ports, N-array ports, and D-Dummy ports. The lens can form M-discrete beams in different angular directions. According to Hansen's proce-

dure for designing Rotman lens, the designer should specify the number of radiating elements (N) to obtain specific gain performance. Also, the spacing (d) between array elements on the array axis, is determined based on the wavelength of a designated frequency, and the desired maximum beam steering angle ($\pm\theta_0$). The radiating element should have a 3dB beam width (BW) greater than or equal ($2\theta_0$). Those are the general requirements of the BFN. Then, the minimum number of Rotman lens beam ports (M) for continuous beamforming is calculated according to the 3dB BW of the resultant N-elements array's pattern for the maximum frequency in the designated band as follows:

$$M = \left\lceil \frac{2\theta_0}{BW_{array}} \right\rceil \tag{1}$$

If Rotman designed with beam-ports less than M, the generated beams would not overlap within 3dB BW of the resultant array pattern, and hence there will be a signal drop while steering process. On the other hand, some applications, like satellite communications, require no overlapping between the generated beams within 3dB BW. The system, in this case, is described as a multibeam rather than beamforming system, where it still can generate beams pointing in different directions, but overlap beyond 3dB BW [7], [19], [20].

After determining the number of beam-ports and array-ports, the parallel-plate waveguide region that connects beam-ports and array-ports is designed based on four significant parameters ($f_1, \alpha, \beta,$ *and* γ). Fig. 1 illustrates these parameters, where f_1 is the (on-axis) focal length, f_2 is the off-axis focal length and are taken from the three points F_0, F_1, and F_2 ("foci") of the beam port contour which is the reference of the input waves and therefore no phase errors. If Rotman lens is fabricated on a dielectric substrate, the substrate permittivity (ε_r) is specified, and the dimensions of the lens are reduced by a factor $\sqrt{\varepsilon_r}$ [29]. For a designated maximum scanning angle θ_0 and specific array length $(N-1)d$, a primary geometrical constraint on the lens on-axis focal length is set to maintain a good amplitude performance and to keep angles and distances between different input and output ports relatively closed to each other [29]:

$$f_1 \gtrsim 2\,(N-1)\,d\,\sin\theta_0 \tag{2}$$

The focal angle α is the angle between the on-axis and off-axis focal lengths and the ratio between them is β.

$$\beta = f_2/f_1 \tag{3}$$

It should be noted that β in Hansen's formulation is the inverse of the original Rotman lens parameter (g). γ is an expansion factor, which is the ratio between the sin of beam steering angle (θ), corresponding to the off-center focal point, and the sin of the focal angle (α) as follows:

$$\gamma = \sin\theta/\sin\alpha \tag{4}$$

y_3 is the position of a typical antenna element on the array axis as shown in Fig. 1. Another critical parameter is the indirect factor of utility ζ, which has a crucial effect on the amplitude and the phase error performance of the lens. ζ is given by

$$\zeta = y_3\gamma/f_1 \tag{5}$$

The last essential parameters for designing Rotman lens are the normalized lengths ($W = w/f_1$) of the transmission lines connecting each array-port to the body of the lens [27].

The effect of those parameters on Rotman lens gain and phase error performance is, briefly, addressed here and summarized in a simple design methodology for optimum mmWaves Rotman lens-based BFN, more details can be found in [27]–[31]. α and β have a similar effect on the geometry of Rotman lens, in which the increase of any one of them, with all other parameters are unchanged, results in opening the beam-ports contour and closing the array-ports contour as depicted in Fig. 2. Despite the effect on the apparent shape of the lens, α and β must be conjunctionally selected with other parameters to obtain an acceptable amplitude performance and minimize the phase aberrations.

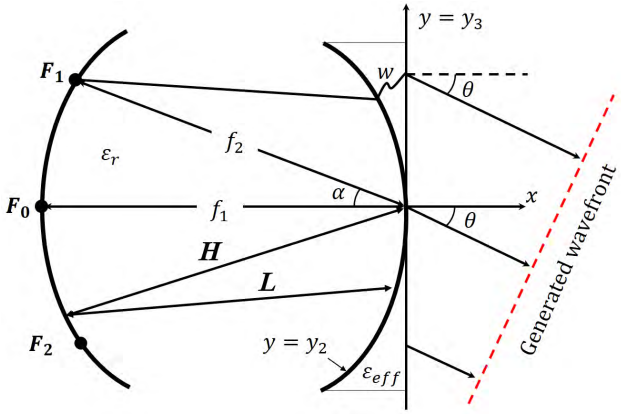

FIGURE 1. Hansen's Modified Rotman Lens.

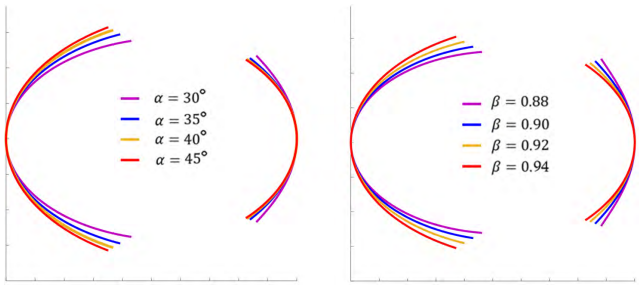

FIGURE 2. Effect of focal angle α and focal ratio β on Rotman lens geometry.

These aberrations are resulted by the difference in path lengths between a central ray of length ($h = H/f_1$) through the center of the array-ports contour and any other ray of length ($l = L/f_1$), both of which are traced from an arbitrary point on the beam-ports contour through the lens and normally terminate to the generated wavefront as shown in Fig. 1. The normalized path difference is a function of both the scan

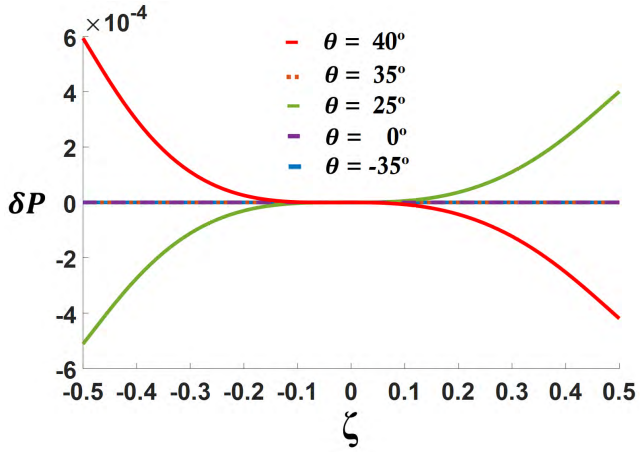

FIGURE 3. Normalized Path difference variation with the location on the array-ports curve for different ray angles. $\alpha = 35°$, $\beta = 0.875$, and $\theta_0 = 45°$.

angle θ and the position along the array contour ζ, and can be derived geometrically [28].

$$\delta P = \sqrt{\varepsilon}_r\,(l-h) + \sqrt{\varepsilon}_e W + y_3 \sin\theta \tag{6}$$

where ε_e is the effective dielectric constant in the transmission lines region. Fig. 3 illustrates the variation of the normalized path difference with ζ for different ray angles θ. It can be seen that the path difference for rays of the focal points ($\theta = 0°$ and $\pm 35°$) is zero, while it increases for rays between foci such as $\theta = 25°$, and even more for rays beyond foci, like the case of ray angle $\theta = 40°$. Therefore, optimization of α and β is needed to minimize the phase error for rays outside foci since they, usually, have larger phase error [27]. Moreover, ζ is bounded by an upper limit which varies with the focal ratio for a given focal angle as shown in Fig. 4. This limit sets a constraint on α and β values during the optimization process. For specific acceptable path difference calculated using (6) and a given $\zeta_{\max}$, an appropriate range of α and β can be chosen from Fig. 4 [27]. Furthermore, various optimization methods can be used to solve the following objective function for α and β which minimize the total absolute path difference for all ports.

$$|\delta P|_{Total} = \sum_{1}^{M}\sum_{1}^{N} \left|\sqrt{\varepsilon}_r\,(l-h) + \sqrt{\varepsilon}_e W + y_3 \sin\theta\right| \tag{7}$$

Some of these methods are based on numerical techniques such as genetic algorithms (GA) [32]. Another method is introduced in [33] based on having three zero error positions on the array axis for each beam port. The presented results in [33] show a considerable path difference reduction compared to [27], [28]. However, the lens performance optimality is not obtained only from the phase error point of view. Amplitude performance, on the other hand, is also an important design factor that must be considered. Without providing both of phase error and amplitude performance together, the picture of BFN performance optimality is somewhat incomplete. For example, Fig.5 shows the path difference for two different $\alpha - \beta$ pairs at the center frequency. Based on (7), the total absolute path difference of $\alpha = 35°$ and $\beta = 0.92$ shown in Fig. 5a is 0.9318, which is better than 1.2092 of $\alpha = 40°$ and $\beta = 0.92$ depicted in Fig. 5b. Furthermore, with $\alpha = 35°$ and $\beta = 0.875$ shown in Fig. 3, the total absolute path difference is 0.7994. However, the path difference minimization does not indicate the whole performance of the BFN, where the gain amplitude performance shown in Fig. 5c indicates that about 4.363 dB amplitude variation between the center beam and the outer one in case of $\alpha = 35°$, $\beta = 0.875$, which is relatively high. This variation is improved to 2.243 dB in case of $\alpha = 35°$ and $\beta = 0.92$, and even better for $\alpha = 40°$ and $\beta = 0.92$ with only 1.754 dB of amplitude variation. In other words, Rotman lens designer should satisfy, for typical applications, a reasonable phase, and amplitude performance together. Table 1 summarizes the amplitude and the total path difference performance for the three $\alpha - \beta$ pairs.

TABLE 1. Path difference and amplitude performance comparison for three $\alpha - \beta$ pairs.

α	β	Total Path difference $\lvert\delta P\rvert_{Total}$	Amplitude Variation (dB)
35°	0.875	0.7994	4.363
35°	0.920	0.9318	2.243
40°	0.920	1.2092	1.754

Other parameters are set to be $\gamma = 1$, $f_1/\lambda = 4$, and $\theta_0 = 45°$

The amplitude performance is approximated by applying aperture theory and uniform distribution to each port, to estimate the amount of electromagnetic (EM) coupling between any two ports [7], [31].

$$S_{ij} = j_o\,(kw_i \sin\phi_i) \times j_o\,(kw_j \sin\phi_j) \times \sqrt{\frac{w_i w_j}{\lambda d_{ij}}}\, e^{-j(k_r d_{ij} + k_e W + \frac{\pi}{4})} \tag{8}$$

$$j_o(x) \equiv \sin(x)/x \tag{9}$$

where k_r and k_e are the phase constants in the parallel plate region and the transmission lines, to the array ports side, region respectively, d_{ij} is the distance between the port i and port j phase centers, w_i, w_j, are the port widths, and ϕ_i, ϕ_j are

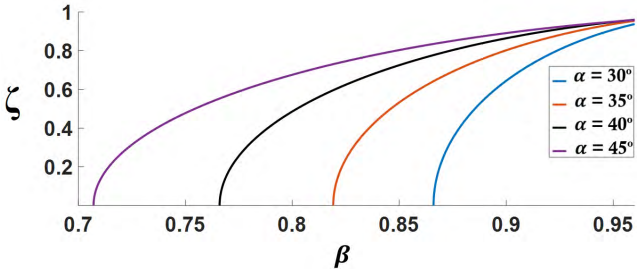

FIGURE 4. Variation of the upper limit on parameter ζ with the focal length for different focal angles.

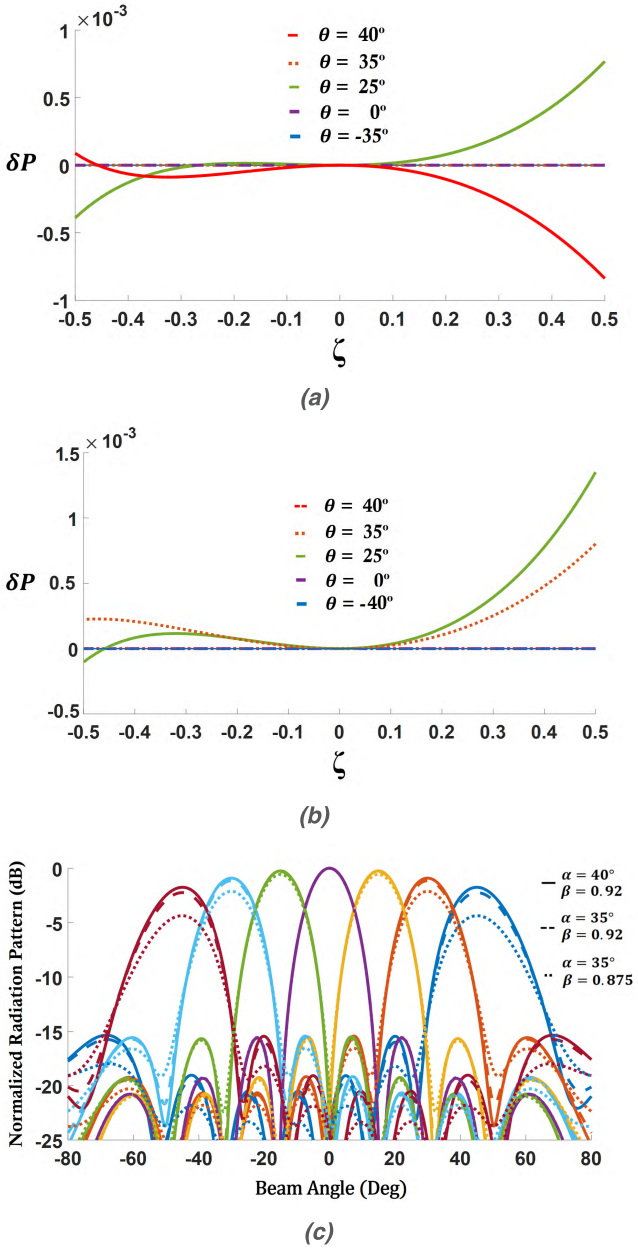

FIGURE 5. Path difference and amplitude performance for different $\alpha - \beta$ pairs: (a) Path difference for $\alpha = 35°$ and $\beta = 0.92$. (b) Path difference for $\alpha = 40°$ and $\beta = 0.92$. (c) Normalized radiation patterns for three different $\alpha - \beta$ pairs. ($\gamma = 1$, $f_1/\lambda = 4$, and $\theta_0 = 45°$).

the angles between the normal to the port aperture and the line connecting the port phase centers.

After obtaining the values of α, β, and ζ, lengths of the transmission lines connected to the array elements are obtained by solving the following quadratic equation [27]:

$$aW^2 + bW + c = 0 \tag{10}$$

where a, b, and c are functions in α, β, and ζ.

The phase centers of the corresponding array ports and beam-ports are obtained using Peter Simon formula [31] Once the phase center coordinates of all beam-ports and array-ports are obtained, a horn of width about ($\lambda/2$) is created around each phase center [27]. The axis of the horn is normal to the port curve. These horns are tapered out of the lens parallel plate region, with a reasonable length, to provide a better impedance match between the feed and lens body. Otherwise, received wave will be transferred into higher order modes in the tapered region and cannot propagate through the feed, but will be reflected [34].

Finally, the side walls of Rotman lens are attached to D number of matched dummy ports to absorb the incoming wave on it and provide a reflection-less termination of the parallel-plate region. There is no specific number of dummy ports that should be selected for Rotman lens design, even in the original proposal of [28]. The vast majority of Rotman lens designs have multiple dummy ports, such as [15]–[19], [32]. On the other hand, some Rotman lens designs adopt only a single dummy port in each side as reported in [20]. According to [35], the side walls curvature, and the dummy ports number and size have some impact on the side lobe level but no visible effect on the main beam. Therefore, dummy ports number, size, and position should be optimized to obtain an acceptable phase and amplitude performance, where they still contribute to the magnitude and phase variation at the array ports due to the multipath reflection. It should be noted that some Rotman lens designs do not employ dummy ports and are replaced by absorbing material [21], [36]. Also because there is some energy lost to the dummy ports, [21] suggests a bed of nails technology to guide the waves instead of dummy ports for effective energy reuse.

B. ROTMAN LENS DESIGN METHODOLOGY

The proposed optimum mmWaves analog beamforming system can be designed according to the following brief and simple designing steps:

1. Select N number of a typical antenna element that has broadband, a wide 3dB BW ($BW_{element}$), and gain performance satisfies the required total array gain.
2. Determine the maximum scanning range ($\pm\theta_0$), provided that $2\theta_0 \leq BW_{element}$ (of the maximum required frequency).
3. Calculate the minimum required number of Rotman lens beam-ports (M) using (1) based on the required application. Note that increasing M increases the scanning accuracy. On the other hand, it increases the mutual coupling between ports.
4. Calculate the minimum required on-axis focal length (f_1) using(2).
5. Calculate the indirect factor of utility ζ using (5) by setting $y_3 = y_{max}$ and $\zeta = \zeta_{\max}$.
6. Choose appropriate values of α and β that satisfy $\zeta_{\max}$ from Fig. 4 as initial guess. Further optimization can be done using (7) and (8) to ensure optimum performance for both of amplitude and phase.

7. Calculate and plot the path difference for the range of $[-\zeta_{max}, \zeta_{max}]$ using (6) and (7). If the path difference exceeds specified maximum permissible limit or amplitude performance declines below a minimum specified level using (8), repeat 6.
8. Solve the quadratic equation (10) to obtain W.
9. Calculate the phase center coordinates for both beam and array ports as in [31].
10. Create a horn of width about $\lambda/2$) around each phase center coordinate with an axis normal to the port curv.
11. Taper the horn, with a reasonable length, toward the feed.
12. Create D number of matched dummy ports at the two side walls of the lens. Otherwise, use absorbing material or guiding structure.

C. ANTENNA DESIGN CONFIGURATION

The single antenna element of the proposed BFN is a Quasi-Yagi antenna of [37]. Unlike the narrowband microstrip patch antenna, this type of antennas provides ultra-wideband that makes it a good selection for TTD beamforming systems. The selected Quasi-Yagi antenna with its dielectric lens follows the endfire radiation antennas' family. Likewise, Vivaldi antenna own ultra-wideband and the endfire radiation. Vivaldi antenna has wider *BW* and broader frequency band than Quasi-Yagi antenna. However, Quasi-Yagi antenna provides higher gain, more compact size, and lighter weight than Vivaldi antenna [38]. Another advantage of the endfire antennas that makes them suitable for planar Rotman lens is their main radiation is less affected by the unwanted radiations, emitted by twisted transmission lines of the array or beam port sides than the broadside antennas, especially at mmWave frequency band. Since one of our main objectives in this paper is to design a compact size BFN, Quasi-Yagi antenna is selected for its compact size, low profile and light-weight in addition to its ultra-wideband. The antenna consists of two major parts as shown in Fig. 6. The first part includes a finite length dipole, reflector, directors and, a transition structure and is located on the top layer of the substrate. On the bottom layer, a U-shaped MS-to-SL balun is placed to feed the driver dipole. This part represents an excitation source for a dielectric slab waveguide (DSW), which is the second part of the antenna. The antenna's input impedance is 50 Ω and is connected to a microstrip line with $w_f = 0.365$mm ($Z_0 = 50$ Ω) followed by another microstrip line of $w_p = 0.178$mm width ($Z_1 = 67$ Ω). This impedance is selected to match the input impedance of the Quasi-Yagi array at the center of the driven element and is usually small, and is strongly influenced by the spacing between the reflector and the driver [39]. The last microstrip line is curved in U-shape to feed the driving dipole through the MS-to-SL transition, providing a single-ended-to-differential conversion with a wide bandwidth. The U-shaped MS-to-SL balun is optimized to achieve a good impedance matching. A dielectric lens enhances the directivity of the Quasi-Yagi antenna with hole slots are inserted in the dielectric substrate to reduce its effective permittivity and consequently, ensure that higher order modes are not excited in the dielectric slab waveguide (DSW) [37].

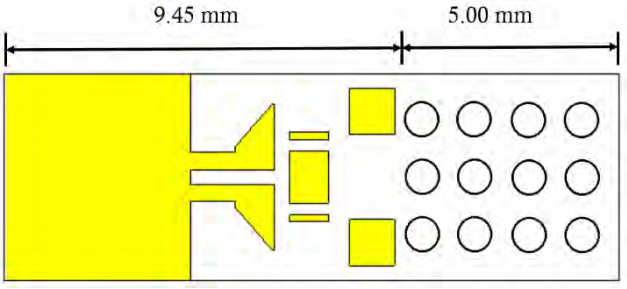

FIGURE 6. Quasi-Yagi antenna for the proposed BFN.

III. SIMULATION RESULTS

Following the calculation and parametric optimization of the lens parameters as discussed in section II, the analog beamforming system is designed with the parameters specified in Table 2. The performance of the beamforming system is evaluated for the single antenna element, lens structure, and the overall integrated beamforming system as follows.

TABLE 2. Main Parameters of the proposed BFN.

Parameter	Symbol	Value
On-axis focal length	f_l	$5\lambda_0$
Focal angle	α	40°
Focal ratio	β	0.9
Expansion Factor	γ	1
Scanning range	$\pm\theta_0$	±40°
Number of Array-ports	N	8
Number of Beam-ports	M	7
Number of Dummy-ports	D	2
Substrate thickness	h	0.381 mm
Total Lens length	l	70.00 mm
Total Lens width	w	50.00 mm
dielectric constant	ε_r	10.2

A. SINGLE ELEMENT

Quasi-Yagi antenna of [37] is designed with lower gain for broader 3dB beamwidth performance so that it allows a wide scanning range. As shown in Fig. 7a, the single element of Quasi-Yagi antenna exhibits broadband of (26-40) GHz. The antenna shows an average gain of 7 dBi and *BW* better than (>83°) in the band (26-34) GHz and gradually decreases to 70° for (34-40) GHz, which is normal due to the larger aperture with respect to operating wavelength as shown in Fig. 7b. This is reflected on the absence of the 3 dB *BW* overlap beyond 34 GHz.

B. ROTMAN LENS

The proposed lens is designed with eight array ports as shown in Fig. 8. The original design requires seven beam-ports,

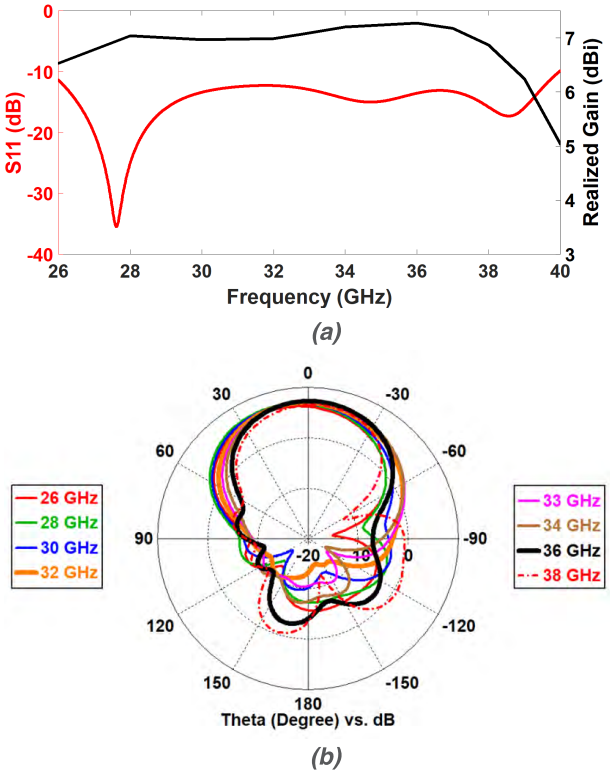

FIGURE 7. Quasi-Yagi antenna performance over (26-38)GHz: (a) Gain and return loss. (b) Radiation patterns.

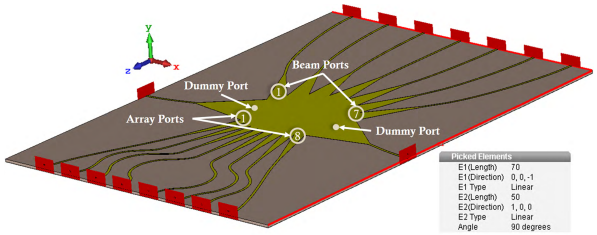

FIGURE 8. Simulated 7 × 8 × 2 Rotman lens design.

according to (1), to steer the beam within a maximum scan angle of $\pm 40°$, and minimum array element spacing of $0.5\lambda_0$. Thus, based on (2) a minimum focal length of $4.5\lambda_0$ is calculated. Therefore, the focal length is set to be $5\lambda_0$. To have equal length transmission lines, so that the system is frequency independent, additional space between the lens array ports and the array antenna elements is necessary.

In our design, the dummy port horn has a wide aperture that assembles having multiply dummy ports at the side walls; this also reduces the number of the dummy loads needed for terminating the side walls of the parallel plate region. The rest of the parameters are selected according to the design methodology in the previous section. The simulation results indicate good impedance matching for the proposed lens, where reflection coefficients of all beam-ports, as illustrated in Fig. 9a, are better than −13 dB. Fig. 9b and Fig 9c show the

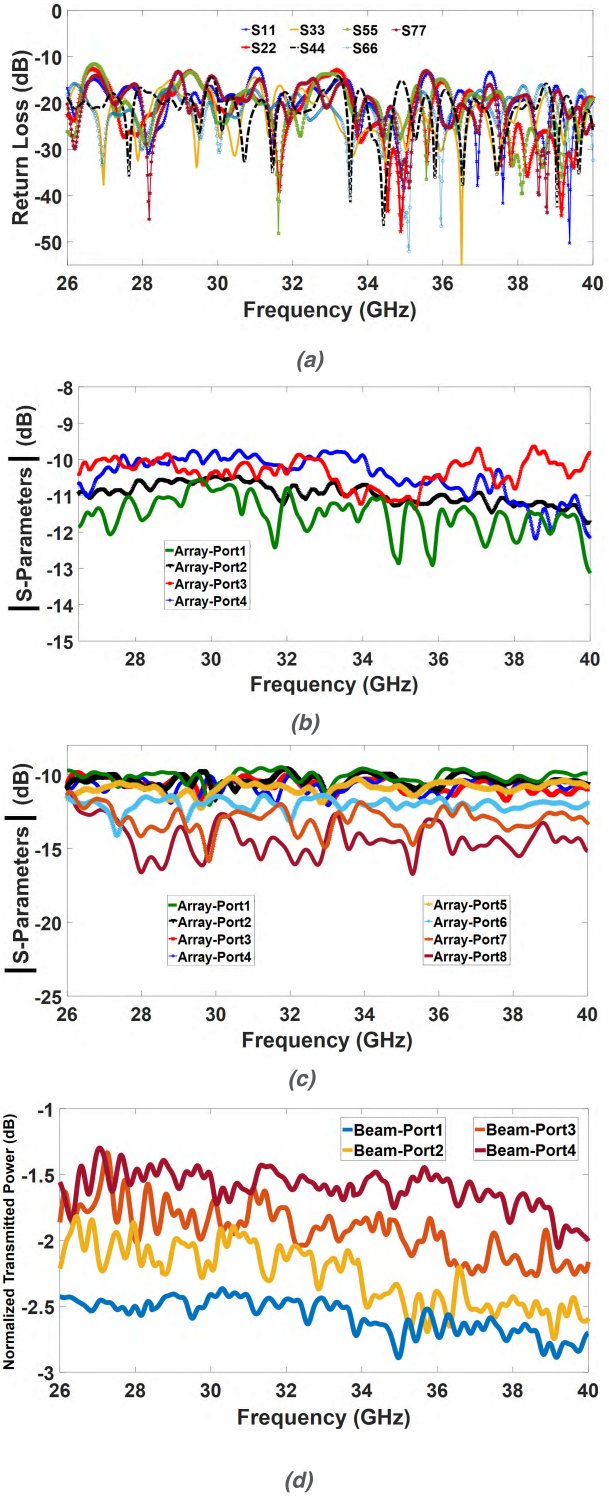

FIGURE 9. S-parameters performance of the proposed Rotman lens: (a) Beam-ports reflection coefficients. (b) Array ports S-Parameters when beam-port 4 is activate, the rest of ports are not shown for symmetry reason. (c) Array ports S-Parameters when beam-port 7 is activate. (d) The normalized transmitted power for each beam port.

magnitude of the S-parameters at the array-ports when they are fed by the center and the edge beam-ports, respectively. The ideal average power level at the eight element array-ports

TABLE 3. Comparison of the proposed beamforming system with other related works.

References	Number of Ports $M\times N\times D$	Frequency GHz	FBW %	Scanning Range degree	Gain dBi	Electrical Size mm^2	Fabrication Technology	Antenna Element
[18]	7×7×8	15.5-16.5	6.25	-30˚ to +30˚	13	5.3 $\lambda_0\times$ 6.4 λ_0	SIW	Vivaldi
[20]	7×15×2	23.6-24.6	4.17	-48˚ to +48˚	22.6	7.2 $\lambda_0\times$ 12 λ_0	SIW	Slotted WG
[23]	5×7×14	26.4-40.1	41.2	-20˚ to +20˚	-	>17.8 $\lambda_0\times$ 17.8 λ_0	RWG	WR28
[24]	11×16×8	60	-	-40˚ to +40˚	-	Not reported	PRGW	-
[21]	5×5×0	6-18	100	-30˚ to +30˚	-	5.2 $\lambda_0\times$ 6.12 λ_0	3D-P-RGW	Double ridge horn
[25]	5×8×8	50-70	33.3	-30˚ to +30˚	-	7.6 $\lambda_0\times$ 8.77 λ_0	inkjet	-
[32]	8×10×28	6-18	100	-28˚ to +28˚	12-20.6	12 $\lambda_0\times$ 12 λ_0	PCB	Double ridge horn
[16]	7×10×8	26-29	10.9	-29˚ to +29˚	14.3	4.0 $\lambda_0\times$ 8.40 λ_0	PCB	Patch
[15]	5×6×4	25-30	18.2	-40˚ to +40˚	-	7.3 $\lambda_0\times$ 11.2 λ_0	PCB	Patch
This work	7×8×2	26-40	42.4	-40˚ to +40˚	14.0	5.5 $\lambda_0\times$ 7.70 λ_0	PCB	Quasi-Yagi

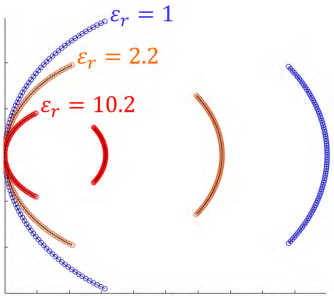

FIGURE 10. The relative size of the proposed Rotman lens with high dielectric material compared to designs with low dielectric constant materials.

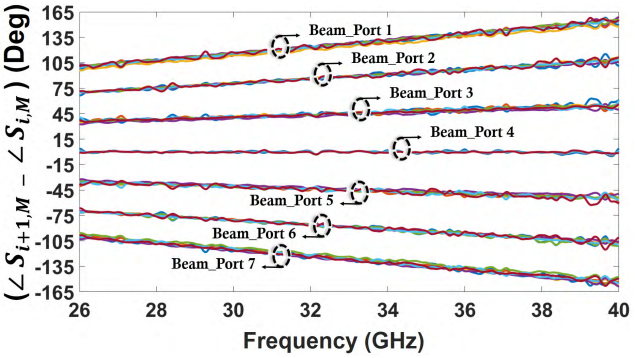

FIGURE 11. The Phase difference between adjacent array ports of the proposed Rotman lens.

fed by the center beam-port, in the absence of material losses, is about −9 dB for each port. However, the selection of, relatively, high dielectric material results in a dielectric loss, in addition to metallic and other types of loss. Also, there is a modest amplitude tapering experienced by array-ports, due to different distances from beam-port. The tapering effect increases when feeding from the edge beam port. All these effects contribute to power level reduction. Consequently, the BFN's gain decreases compared to the gain of ideal N element, uniformly excited and equally spaced linear array. The relative total transmitted power accounts for all types of loss and is calculated using the simulated S-parameter of all array-ports fed by each beam-port as follows [19]

$$P_j = \sum_{i=1}^{N} |S_{ij}|^2, \quad j= 1, 2, \ldots M \tag{11}$$

The proposed BFN has good S-parameters magnitude at the array-ports, with a relative transmitted power level ranges

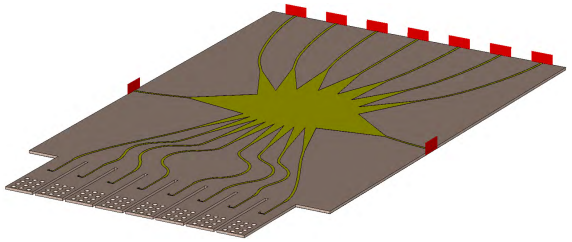

FIGURE 12. Integration of the antenna array with Rotman lens.

between −1.5 dB to −2.9 dB over 26-40 GHz as shown in Fig. 9d. The rest of the ports are not reported for symmetry reason. These levels indicate an efficiency above 71% for the center beam-port, 60.3% for beam-port 3, 55% for beam-port 2, and 51.3% for beam-port 1. These losses are expected as discussed and increase unavoidably with the

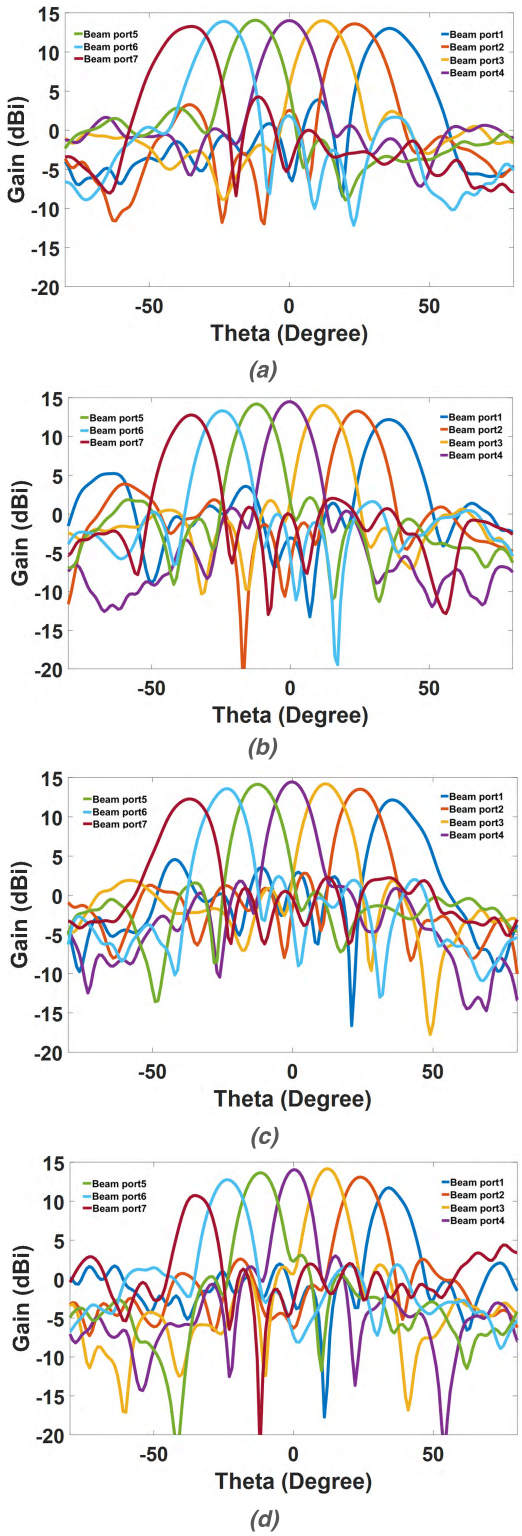

FIGURE 13. Simulated Radiation patterns of the proposed BFN: (a) 26 GHz (b) 28 GHz. (c) 32 GHz. and (d) 38 GHz.

increase of the scanning angle, especially, at higher frequencies. However, the lens size is tremendously reduced compared to air-filled or low dielectric material Rotman lens design as shown in Fig. 10.

The phase distributions across the array-ports show a linear behavior as depicted in Fig. 11. Although the phase error of the three focal points is theoretically zero, the multipath reflection might result in some phase deviation. The phase error for the center beam-port is about $\pm 3.5°$, increases to the maximum phase error of $\pm 6.6°$ for beam-port 1 due to the multipath reflection and the mutual coupling between adjacent ports. A phase error of $\pm 5.4°$ is for beam-port 2 and $\pm 6.2°$, for beam-port 3. Nevertheless, the radiation patterns, in the next section, indicate that the phase error is still within an acceptable range.

C. ROTMAN LENS-BASED BEAMFORMING SYSTEM

Eight Quasi-Yagi antennas are integrated with the proposed lens as shown in Fig. 12. The main beam points at seven different angular directions, as shown in Fig. 13 covering the range of $\pm 40°$. The beam directions are uniformly distributed at $\pm 40°$, $\pm 26.7°$, $\pm 13.33°$, and $0°$. The maximum achieved simulated realized gain is 14.5 dBi at 28 GHz for the center beam. There is a side lobe of a significant level (SLL ~ -9 dB) when beam-port 1 is activated at 28 GHz, however, it is out of the designated field-of-view. The radiation patterns of 38 GHz show a gain drop beyond 3dB at $\pm 40°$ due to the single antenna element's 3dB *BW*, as explained previously in section A.

IV. EXPERIMENTAL RESULTS AND MANUFACTURING

To validate the proposed analog BFN, Rotman lens with seven input ports feeding eight Quasi-Yagi antenna array is fabricated and tested as shown in Fig. 14. The lens is 50mm

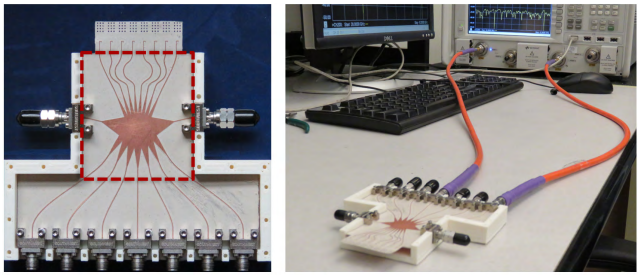

FIGURE 14. Proposed BFN prototype.

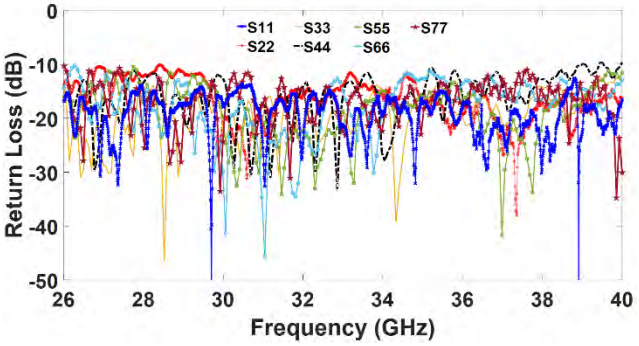

FIGURE 15. Measured reflection coefficients of the proposed BFN.

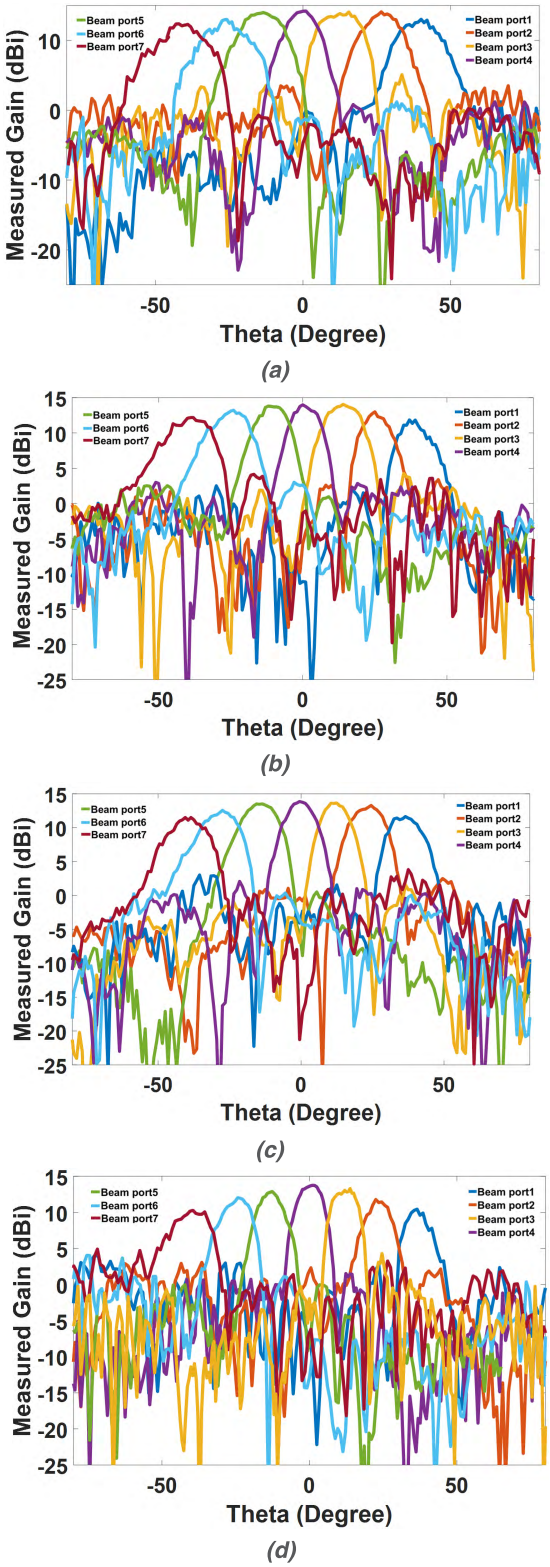

FIGURE 16. Measured Radiation patterns of the proposed BFN: (a) 26 GHz (b) 28 GHz. (c) 32 GHz. and (d) 38 GHz.

by 70mm size. The measured reflection coefficients depicted in Fig. 15 show good impedance matching below −10 dB over a broad frequency band (26-40) GHz, for all beam-ports. The maximum measured gain for the center beam is about 14 dBi at 28 GHz. The radiation patterns shown in Fig.16 validate the system steering capability by providing beams at −39.7°, −26.5°, −13.3°, 0°, +13.3°, +26.5°, and +39.5°.

The radiation patterns have some ripples, especially for the wide angle rays, this is due to some imperfections of the chamber room. The steered beam radiation patterns are vulnerable to such ripples due to the contribution of their side lobes to multipath reflection from different walls of the chamber room, while the central beam has no or less ripples.

It can be seen from Fig. 9a, Fig. 13, Fig. 15 and Fig. 16 that the simulation and measurement results are in a good agreement. Measured gain is slightly less than the simulated one and ranges between 13.8 to 14 dBi. This difference might be caused by the excessive dielectric losses in the additional length that is needed to separate the connectors at the input port side, and also the use of the end lunch connector to excite the microstrip line introduces additional losses. However, the measured results are quite encouraging taking into account the misalignment losses. The proposed analog BFN is compared to some relevant works as summarized in Table 3. It exhibits a reasonable gain level, especially with its compact size. It is smaller than all systems mentioned in Table 3 except [18] and [21] but is better than both of them for its low-cost, low profile, and extremely light-weight. In addition, the proposed system has a better broadband than [18] with more than 42% FBW. Besides, the proposed system has a wide scanning range of ±40° which is better than most of the relevant systems in Table 3. Reference [20] has wider scanning range and a quite high gain but is very narrowband with only 4.17 % FBW. References [21] and [32] present BFN systems of 100% FBW, which is really a quite broadband, but they have a low scanning range ($|\theta_0| \leq 30°$) compared to the proposed system in this paper.

V. CONCLUSION

An analog beamforming system using a compact-size Rotman lens fed eight Quasi-Yagi antenna array for 5G and mmWave applications is presented. The proposed system is fabricated using standard planar low-cost processing PCB technology for MMIC in the 26-40 GHz band. The antenna and the beamforming system design methodology is described in details, and its performance is confirmed experimentally. The system exhibits good impedance matching and beam steering capability. A range of ±40° is achieved which is better than most of the relevant systems in Table 3. The BFN bandwidth ($S_{11} < -10$ dB) is larger than 42 % and is limited by the single antenna element bandwidth. With such performance and compactness, the proposed system is qualified for a wide range of potential 5G applications such as the advanced MIMO and hybrid beamforming systems.

REFERENCES

[1] T. S. Rappaport *et al.*, "Millimeter wave mobile communications for 5G cellular: It will work!" *IEEE Access*, vol. 1, pp. 335–349, 2013.

[2] T. Inoue, "5G standards progress and challenges," in *Proc. IEEE Radio Wireless Symp. (RWS)*, Phoenix, AZ, USA, Jan. 2017, pp. 1–4. doi: 10.1109/RWS.2017.8048566.
[3] D. Liu, W. Hong, T. S. Rappaport, C. Luxey, and W. Hong, "What will 5G antennas and propagation be?" *IEEE Trans. Antennas Propag.*, vol. 65, no. 12, pp. 6205–6212, Dec. 2017. doi: 10.1109/TAP.2017.2774707.
[4] J. Lian, Y. Ban, C. Xiao, and Z. Yu, "Compact substrate-integrated 4×8 butler matrix with sidelobe suppression for millimeter-wave multi-beam application," *IEEE Antennas Wireless Propag. Lett.*, vol. 17, no. 5, pp. 928–932, May 2018. doi: 10.1109/LAWP.2018.2825367.
[5] Y. Cao, K.-S. Chin, W. Che, W. Yang, and E. S. Li, "A compact 38 GHz multibeam antenna array with multifolded butler matrix for 5G applications," *IEEE Antennas Wireless Propag. Lett.*, vol. 16, pp. 2996–2999, 2017. doi: 10.1109/LAWP.2017.2757045.
[6] Y. J. Cho, G.-Y. Suk, B. Kim, D. K. Kim, and C.-B. Chae, "RF lens-embedded antenna array for mmWave MIMO: Design and performance," *IEEE Commun. Mag.*, vol. 56, no. 7, pp. 42–48, Jul. 2018. doi: 10.1109/MCOM.2018.1701019.
[7] A. Rahimian, "Design and performance of a Ku-band Rotman lens beamforming network for satellite systems," *Prog. Electromagn. Res. B*, vol. 28, pp. 41–55, Jan. 2013. doi: 10.2528/PIERM12111511.
[8] Y. Liu, H. Yang, D. Huang, and J. Zhu, "A low sidelobe multi-beam slot array antenna fed by Rotman lens," in *Proc. Loughborough Antennas Propag. Conf. (LAPC)*, Loughborough, Nov. 2016, pp. 1–5. doi: 10.1109/LAPC.2016.7807502.
[9] A. Pautz, M. Hägelen, and R. Kulke, "Multiple target detection using Rotman lens beamforming," in *Proc. 18th Int. Radar Symp. (IRS)*, Prague, Czech Republic, Jun. 2017, pp. 1–10. doi: 10.23919/IRS.2017. 8008178.
[10] O. Kilic and S. J. Weiss, "Rotman lens applications for the US Army: A review of history, present, and future," *URSI Radio Sci. Bull.*, vol. 2010, no. 332, pp. 10–23, Jun. 2010. doi: 10.23919/URSIRSB.2010.7909283.
[11] E. Tolin, O. Litschke, S. Bruni, and F. Vipiana, "Innovative Rotman lens setup for extended scan range array antennas," in *Proc. IEEE-APS Top. Conf. Antennas Propag. Wireless Commun. (APWC)*, Verona, Italy, Sep. 2017, pp. 252–255. doi: 10.1109/APWC.2017.8062294.
[12] B. Jlassi. (2018). MEMS-Based Millimeter Front-end for Automotive Radar Applications. UWSpace. [Online]. Available: https://uwspace.uwaterloo.ca/handle/10012/12890
[13] R. Rotman, M. Tur, and L. Yaron, "True time delay in phased arrays," *Proc. IEEE*, vol. 104, no. 3, pp. 504–518, Mar. 2016. doi: 10.1109/JPROC.2016.2515122.
[14] X. Wang, A. Akbarzadeh, L. Zou, and C. Caloz, "Real-time spectrum sniffer for cognitive radio based on Rotman lens spectrum decomposer," *IEEE Access*, vol. 6, pp. 52366–52373, 2018. doi: 10.1109/ACCESS.2018.2870562.
[15] M. A. Hassanien, R. Hahnel, and D. Plettemeier, "A novel electronically wideband steering system using Rotman lens for 5G applications at 28 GHz," in *Proc. 12th Eur. Conf. Antennas Propag. (EuCAP)*, London, U.K., 2018, pp. 1–5. doi: 10.1049/cp.2018.1001.
[16] T. K. V. Dai, T. Nguyen, and O. Kilic, "Compact multi-layer microstrip Rotman lens design using coupling slots to support millimetre wave devices," *IET Microw., Antennas Propag.*, vol. 12, no. 8, pp. 1260–1265, Jan. 2018. doi: 10.1049/iet-map.2017.0817.
[17] J. Pourahmadazar and T. Denidni, "X-band substarte integrated Rotman Lens with ±24° scanning capability," in *Proc. IEEE Int. Symp. Antennas Propag. USNC/URSI Nat. Radio Sci. Meeting*, Vancouver, BC, Canada, Jul. 2015, pp. 232–233. doi: 10.1109/APS.2015.7304502.
[18] S. A. R. Hosseini, Z. H. Firouzeh, and M. Maddahali, "Design of Rotman lens antenna at Ku-band based on substrate integrated technology," *J. Commun. Eng.*, vol. 3, no. 1, pp. 33–43, Jan./Jun. 2014.
[19] K. Tekkouk, M. Ettorre, L. Le Coq, and R. Sauleau, "Multibeam SIW slotted waveguide antenna system fed by a compact dual-layer Rotman lens," *IEEE Trans. Antennas Propag.*, vol. 64, no. 2, pp. 504–514, Feb. 2016. doi: 10.1109/TAP.2015.2499752.
[20] K. Tekkouk, M. Ettorre, and R. Sauleau, "SIW Rotman lens antenna with ridged delay lines and reduced footprint," *IEEE Trans. Microw. Theory Techn.*, vol. 66, no. 6, pp. 3136–3144, Jun. 2018. doi: 10.1109/TMTT.2018.2825374.
[21] K. V. Hoel, S. Kristoffersen, N. Jastram, and D. S. Filipovic, "3D printed Rotman lens," in *Proc. 47th Eur. Microw. Conf. (EuMC)*, Nuremberg, Germany, Oct. 2017, pp. 125–128. doi: 10.23919/EuMC.2017.8230815.
[22] L. F. C. Suárez, D. V. N. Méndez, M. Baquero-Escudero, B. Bernardo-Clemente, and S. M. Giner, "Transitions between Gap Waveguides for use in a phased array antenna fed by a Rotman lens," in *Proc. 8th Eur. Conf. Antennas Propag. (EuCAP)*, The Hague, The Netherlands, Apr. 2014, pp. 774–777. doi: 10.1109/EuCAP.2014.6901875.
[23] F. C. Suárez, D. N. Méndez, and M. Baquero-Escudero, "Rotman lens with ridge gap waveguide technology for millimeter wave applications," in *Proc. 7th Eur. Conf. Antennas Propag. (EuCAP)*, Gothenburg, Sweden, Apr. 2013, pp. 4006–4009.
[24] J. Pourahmadazar, M. Farahani, and T. Denidni, "Printed ridge gap waveguide Rotman lens for millimetre-wave applications," in *Proc. 18th Int. Symp. Antenna Technol. Appl. Electromagn. (ANTEM)*, Waterloo, ON, Canada, Aug. 2018, pp. 1–2. doi: 10.1109/ANTEM.2018.8572972.
[25] A. Rahimian, A. Alomainy, and Y. Alfadhl, "A flexible printed millimetre-wave beamforming network for WiGig and 5G wireless subsystems," in *Proc. Loughborough Antennas Propag. Conf. (LAPC)*, Loughborough, U.K., Nov. 2016, pp. 1–5. doi: 10.1109/LAPC.2016.7807565.
[26] *Setting the Scene for 5G: Opportunities & Challenges*. Accessed: Jan. 15, 2019. [Online]. Available: https://www.itu.int/en/ITU-D/Documents/ITU_5G_REPORT-2018.pdf
[27] R. C. Hansen, "Design trades for Rotman lenses," *IEEE Trans. Antennas Propag.*, vol. 39, no. 4, pp. 464–472, Apr. 1991. doi: 10.1109/8.81458.
[28] W. Rotman and R. Turner, "Wide-angle microwave lens for line source applications," *IEEE Trans. Antennas Propag.*, vol. AP-11, no. 6, pp. 623–632, Nov. 1963.
[29] M. S. Smith, "Design considerations for Ruze and Rotman lenses," *Radio Electron. Eng.*, vol. 52, no. 4, pp. 181–187, Apr. 1982. doi: 10.1049/ree.1982.0027.
[30] T. Katagi, S. Mano, and S. Sato, "An improved design method of Rotman lens antennas," *IEEE Trans. Antennas Propag.*, vol. 32, no. 5, pp. 524–527, May 1984. doi: 10.1109/TAP.1984.1143353.
[31] P. Simon, "Analysis and synthesis of Rotman lenses," in *Proc. 22nd AIAA Int. Commun. Satell. Syst. Conf. Exhib. (ICSSC)*, May 2004, p. 3196. doi: 10.2514/6.2004-3196.
[32] A. Darvazehban, O. Manoochehri, M. A. Salari, P. Dehkhoda, and A. Tavakoli, "Ultra-wideband scanning antenna array with rotman lens," *IEEE Trans. Microw. Theory Techn.*, vol. 65, no. 9, pp. 3435–3442, Sep. 2017. doi: 10.1109/TMTT.2017.2666810.
[33] R. Uyguroglu and A. Y. Oztoprak, "A method for minimizing the phase errors of Rotman lenses," in *Proc. Int. Conf. Elect. Electron. Eng. (ELECO)*, Bursa, Malaysia, Nov. 2009, pp. II-174–II-176.
[34] E. O. Rausch and A. F. Peterson, "Rotman lens design issues," in *Proc. IEEE Antennas Propag. Soc. Int. Symp.*, Washington, DC, USA, vol. 2B, Jul. 2005, pp. 35–38. doi: 10.1109/APS.2005.1551928.
[35] C. W. Penney, "Rotman lens design and simulation in software [application notes]," *IEEE Microw. Mag.*, vol. 9, no. 6, pp. 138–149, Dec. 2008. doi: 10.1109/MMM.2008.929774.
[36] E. Sbarra, L. Marcaccioli, R. V. Gatti, and R. Sorrentino, "A novel Rotman lens in SIW technology," in *Proc. Eur. Radar Conf.*, Munich, Germany, Oct. 2007, pp. 236–239. doi: 10.1109/EURAD.2007.4404980.
[37] E. H. Mujammami and A. B. Sebak, "Wideband high gain printed Quasi-Yagi diffraction gratings-based antenna for 5G applications," *IEEE Access*, vol. 7, pp. 18089–18100, 2019. doi: 10.1109/ACCESS.2019.2897092.
[38] M. Yunita, G. Hadi, Y. Isvara, A. Budiyarto, and A. Budiyono, "Analysis of Vivaldi, rectangular, bow-tie, and Quasi-Yagi antenna performance for S-band FMCW-SAR on UAV platform," *J. Unmanned Syst. Technol.*, vol. 5, no. 3, pp. 76–79, 2018. doi: 10.21535/just.v5i3.976.
[39] C. A. Balanis, *Antenna Theory Analysis and Design*, 3rd ed. Hoboken, NJ, USA: Wiley, 2005.

ESSA H. MUJAMMAMI (GS'18) received the B.Sc. and M.Sc. degrees in electrical engineering from King Saud University, Riyadh, Saudi Arabia, in 2001 and 2006, respectively. He is currently pursuing the Ph.D. degree in electrical and computer engineering with Concordia University, Montreal, QC, Canada. His research interests include millimeter-wave, microwave components and antennas. He was an Electrical Engineer of the General Directorate of Communication, Ministry of Interior (MOI), Saudi Arabia, from 2008 to 2010. He was the Director of ICT, MOI, from 2010 to 2014.

ISLAM AFIFI (GS'18) received the B.Sc. degree in electronics and communication engineering and the M.Sc. degree in engineering physics from Cairo University, Cairo, Egypt, in 2009 and 2014, respectively. He is currently pursuing the Ph.D. degree in electrical and computer engineering with Concordia University, Montreal, QC, Canada. He was a Teaching and Research Assistant with the Engineering Mathematics and Physics Department, from 2009 to 2014, and a Senior Teaching Assistant, from 2014 to 2016. His research interests include millimeter-wave microwave components and antennas.

ABDELRAZIK B. SEBAK (LF'18) received the B.Sc. degree (Hons.) in electrical engineering from Cairo University, Cairo, Egypt, in 1976, the B.Sc. degree in applied mathematics from Ain Shams University, Cairo, in 1978, and the M.Eng. and Ph.D. degrees in electrical engineering from the University of Manitoba, Winnipeg, MB, Canada, in 1982 and 1984, respectively. From 1984 to 1986, he was with Canadian Marconi Company, where he was involved in the design of microstrip phased array antennas. From 1987 to 2002, he was a Professor with the Department of Electronics and Communication Engineering, University of Manitoba. He is currently a Professor with the Department of Electrical and Computer Engineering, Concordia University, Montreal, QC, Canada. His research interests include phased array antennas, millimeter-wave antennas and imaging, computational electromagnetics, and interaction of electromagnetic (EM) waves with engineered materials and bioelectromagnetics. He is a member of the Canadian National Committee of International Union of Radio Science Commission B. He was a recipient of the 2000 and 1992 University of Manitoba Merit Award for Outstanding Teaching and Research, the 1994 Rh Award for Outstanding Contributions to Scholarship and Research, and the 1996 Faculty of Engineering Superior. He has served as the Chair for the IEEE Canada Awards and Recognition Committee, from 2002 to 2004, and as the Technical Program Chair for the 2002 IEEE CCECE Conference and the 2006 URSI ANTEMS Symposium. He is a Technical Program Co-Chair of the 2015 IEEE ICUWB Conference.